MNRAS 000, 1–9 (2016) Preprint 22 August 2016 Compiled using MNRAS LATEX style file v3.0

The wild west of the Orion Nebula

Alba Fernández-Martín ,[1⋆] William J. Henney,[1] M. Teresa García-Díaz[2] and S. Jane Arthur[1]
[1]*Instituto de Radioastronomía y Astrofísica, UNAM, Apartado Postal 3-72, 58090 Morelia, Michoacán, México*
[2]*Instituto de Astronomía, UNAM, Km 103 Carretera Tijuana-Ensenada, 22860 Ensenada, Baja California, México*

Accepted XXX. Received YYY; in original form ZZZ

ABSTRACT
Single paragraph,not more than 250 words and no references.
Aims.
Methods.
Results.

Key words: keyword1 – keyword2 – keyword3 – keyword4 – keyword5 – keyword6

1 INTRODUCTION

Describir LL1, LL2 y LL3, si no poner sus referencias en la seccion 3.

2 OBSERVATIONS AND DATA REDUCTION

2.1 Observations

High-resolution spectroscopic observations were obtained at the 2.1-m telescope of the Observatorio Astronómico Nacional San Pedro Mártir (Baja California, México) in a f/7.5 configuration using the MES-SPM instrument (Manchester Echelle Spectrometer; Meaburn et al. 2003). A total of 56 positions were obtained from seven sets of observations carried out in 2006, 2007, 2010, 2013 and 2015. The number of positions acquired in each set of observations, dates, exposition times and airmass during the observations are summarized in Table 1.

For the 2006, 2007a, 2007b and 2010 observations the instrument was equipped with the detector SITE-3 CCD, which is an array of 1024×1024 (24μm) pixels giving a spatial resolution of 0.321 arcsec/pix (without considering the binning). On the other hand, the CDD for the 2013a, 2013b and 2015 sets, Marconi-2, was a detector with 2048×2048 square pixel, each 13.5 μm, giving a spatial resolution of 0.176 arcsec/pix (without considering the binning). The slit width was set at 150μ (1.95 arcsec on the sky) throughout the observation and it was oriented in the north-south direction for 2006, 2007a, 2007b and 2010 observations and in the east-west direction for the 2013a, 2013b and 2015 ones.

In order to establish the exact position of the slit in each pointing we took direct slit images of short duration, in which the diffraction grating was replaced by a mirror. Additionally, thorium-argon lamp spectra were taken for wavelength calibration between each slit position.

Finally, taking the seven data sets into account, we get 56 slit-positions in Hα, [N II]λ6548 and [N II]λ6584, lines spanning an interval of 217 arcmin in RA and 9 arcmin in DEC. In addition, exposures in [S II]λ6717 and [S II]λ6730Å were also observed in four pointings and [O III]λ5007 in one position, as indicated in Table 1. In order to illustrate the spatial distribution of the observations in Fig. 1 we show the 56 slit positions observed in Hα+[N II] plotted over an Hα image obtained from Da Rio et al. (2009).

2.2 Data reduction

The spectra were reduced using IRAF[1] by following the standard procedure for 2D spectroscopic observations (bias subtraction, flat-fielding and cosmic ray removal). The wavelength calibration was performed using thorium-argon arcs taken between each slit position.

After transforming all the spectra to a common heliocentric velocity frame, we performed a series of further corrections to obtained well calibrated spectra in a self-consistent way.

⋆ E-mail: a.fernandez@crya.unam.mx

[1] The Image Reduction and Analysis Facility IRAF is distributed by the National Optical Astronomy Observatories, which are operated by Association of Universities for Research in Astronomy, Inc., under cooperative agreement with the National Science Foundation.

Table 1. Summary of the data set observed with the spectrograph MES-SPM.

Set name	Dates	# Slits[a]	Orientation	Spatial resolution[b] (arcsec pix^{-1})	Cover area (arcmin^2)	Exp. time[c] (s)	Airmass[d]
2006	2006 Feb 5	11/0/0	Vertical	0.624	6×6	300(3)/600(8)	1.68
2007a	2007 Jan 10	3/1/1	Vertical	0.624	2×6	600	1.67
2007b	2007 Jan 13	7/0/0	Vertical	0.624	14×6	600	1.30
2010	2010 Jan 15,16,17	17/3/1	Vertical	0.624	17×6	450(1)/600(20)	1.37
2013a	2013 Feb 16,18,19	11/0/0	Horizontal	0.527	100×2	450(1)/600(10)	1.52
2013b	2013 Dec 11	5/0/0	Horizontal	0.527	114×0.2	600	1.49
2015	2015 Feb 3	2/0/0	Horizontal	0.351	88×0.2	600	1.29

[a] Number of slit positions observed in Hα+[N II]$\lambda\lambda$6548,6584 / [S II]$\lambda\lambda$6717,6731 / [O III]λ5007.

[b] Final spatial resolution taking the spatial binning into account.

[c] 2006, 2010 and 2013a spectra were taken with different exposition times (separated by a bar). Number of position acquired with each exposition time are indicated in brackets. This was taking into account when combining images in the data reduction.

[d] Mean value during the observations.

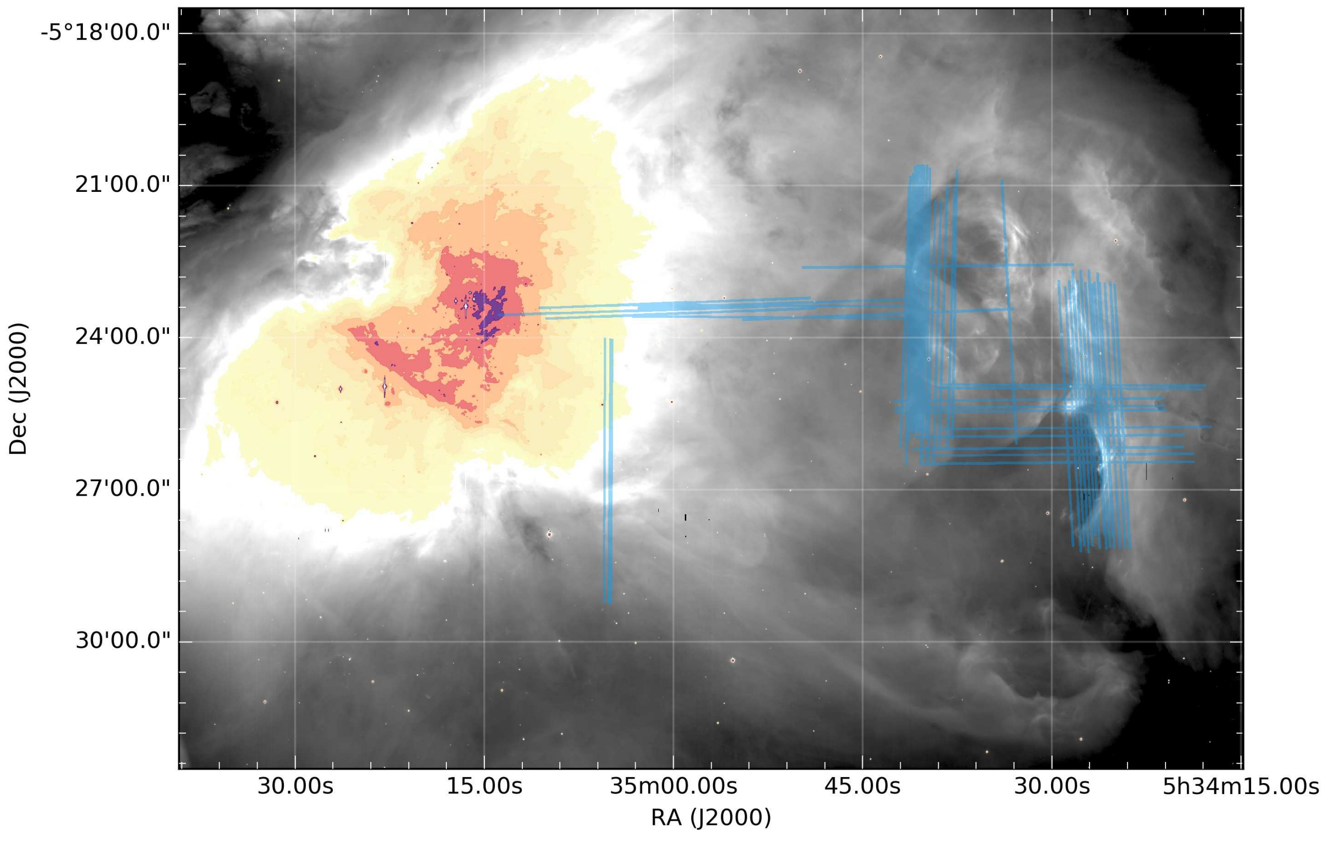

Figure 1. Positions and orientations of the spectroscopic settings observed in Hα+[N II] with MES-SPM (in blue) poltted over the Hα image of the western region of the Orion nebula obtained from Da Rio et al. (2009). North is up and east to the left.

(i) An astrometric solution was found for each of the spectra using nearby stars. This allowed us to accurately determine the slit position of each exposure.

(ii) In order to compensate the variations in the sky transparency and seeing between exposures we compare our spectra with a deep Hα image of the region obtained from Da Rio et al. (2009) with the Wide Field Imager (WFI) at the 2.2-m MPG/ESO telescope at La Silla. This was done by fitting a low-order Chebyshev polynomial to the spectra to WFI profile ratio. With this we obtained a brightness normalization factor for each spectra, as well as a correction for flux gradients along the slits. The corrections are typically lower than 15 percent. This comparison also allowed us to flux-calibrate our spectra, using the spectrophotometry provided by Weilbacher et al. (2015) with MUSE in common regions. Figure 2 shows a three-panel plot with the flux calibration for one of the positions.

(iii) Continuum emission was removed by fitting a two-

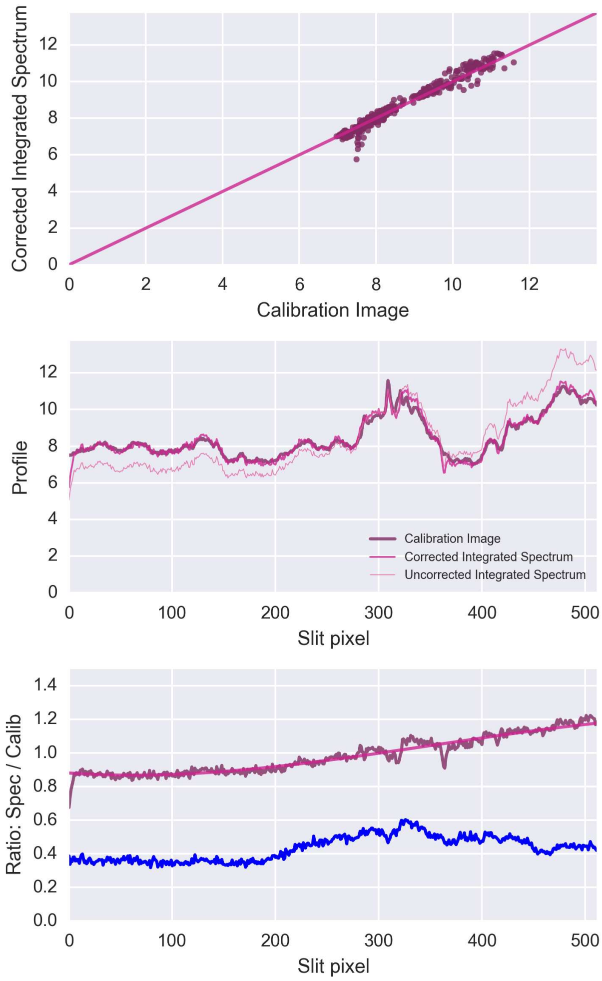

Figure 2. Example of flux-calibration of one of the 2006 spectra in Hα. Top panel: calibrated spectrum profile plotted against calibration WFI image profile. Centre panel: corrected, uncorrected and calibration WFI spectra profiles along the slit. Bottom panel: Chebyshev polynomial function used for calibration (**COLOUR?**), spectrum-WFI ratio corrected (pink) and uncorrected (blue) plotted along the slit. **(YO: ponemos esta figura?. WILL: rehacer colores)**

dimensional Chebyshev function. For each exposure a background section was selected including only line-free regions of the spectrum (we use an excluded velocity window of -10 to +40 $\mathrm{km\,s^{-1}}$in heliocentric velocity around the line core). In addition we use an intensity threshold to distinguish high velocity knots from noise.

Figure 3 shows the resultant calibrated two-dimensional spectra in Hα (top row) and [N II] (bottom row) for three representative slit positions.

2.3 Isovelocity maps

In order to better reveal the spatio-kinematical patterns in the observed region, the slit spectra were combined and interpolated to produce isovelocity channel maps. To that end, we carried out the following steps.

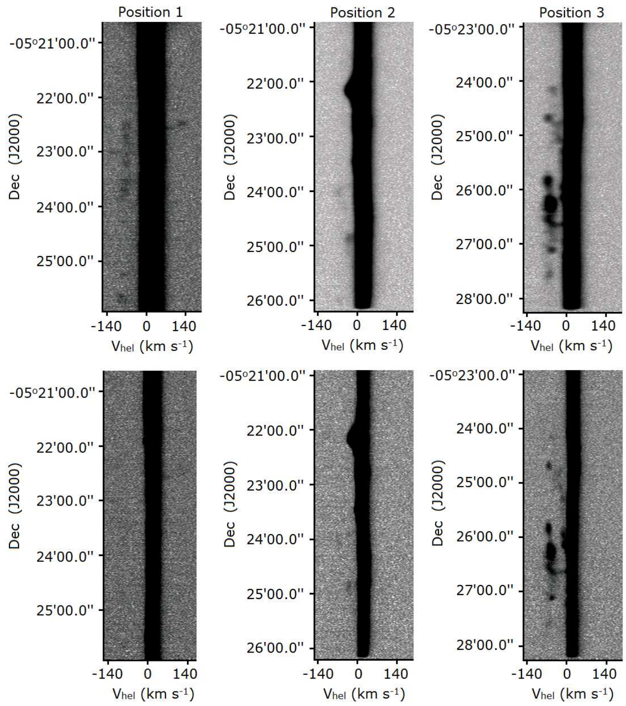

Figure 3. Calibrated two-dimensional spectra for three representative slit positions. The top row shows the Hα emission line and the bottom one the [N II]λ6584 emission line.

First, we built an orthogonal RA-DEC grid placing all the slits onto there by looping over slit profiles extracted in a given wavelength (helocentric velocity) window. On those grid pixels in which two or more slits fall, the intensity was estimated as the mean weighted by the slit quality. Grid pixels where no slit falls were left transparent.

Due to observational differences between each set of observations (i.e. spatial resolution and seeing) we generated multi-resolution maps in order to not degrade the quality of the better spectra. To do that, we build several isovelocity maps onto grids with binning of 2 (better resolution), 4, 8, 16 and 32 (worst resolution).

Finally, all the grids were combined to obtain multigrid smoothed channel maps with a spatial resolution ranging from 0.5 to 15.1 $\mathrm{arcsec\,pix^{-1}}$. We created maps in several velocity ranges to find kinematical structures at different velocities: the narrow band channels cover velocities from -10 to -110 $\mathrm{km\,s^{-1}}$and from +10 to +170 $\mathrm{km\,s^{-1}}$ in steps of 20 $\mathrm{km\,s^{-1}}$, while the wide bands span from +0 to +60, -60 to +0 and -120 to -60 $\mathrm{km\,s^{-1}}$. The line core is also sampled in the channel ranging from -10 to +10 $\mathrm{km\,s^{-1}}$. These isovelocity maps were performed only in Hα and [N II] emission lines, because in [S II] and [O III] the spatial coverage of the observations is too small.

A particularly useful method of identifying large-scale velocity systems is to study images that are color-coded to simultaneously show different velocity ranges. Taking this idea into account we show in Figure 4 a combined isovelocity channel maps for Hα.

The analysis of the isovelocity channel maps reveal a

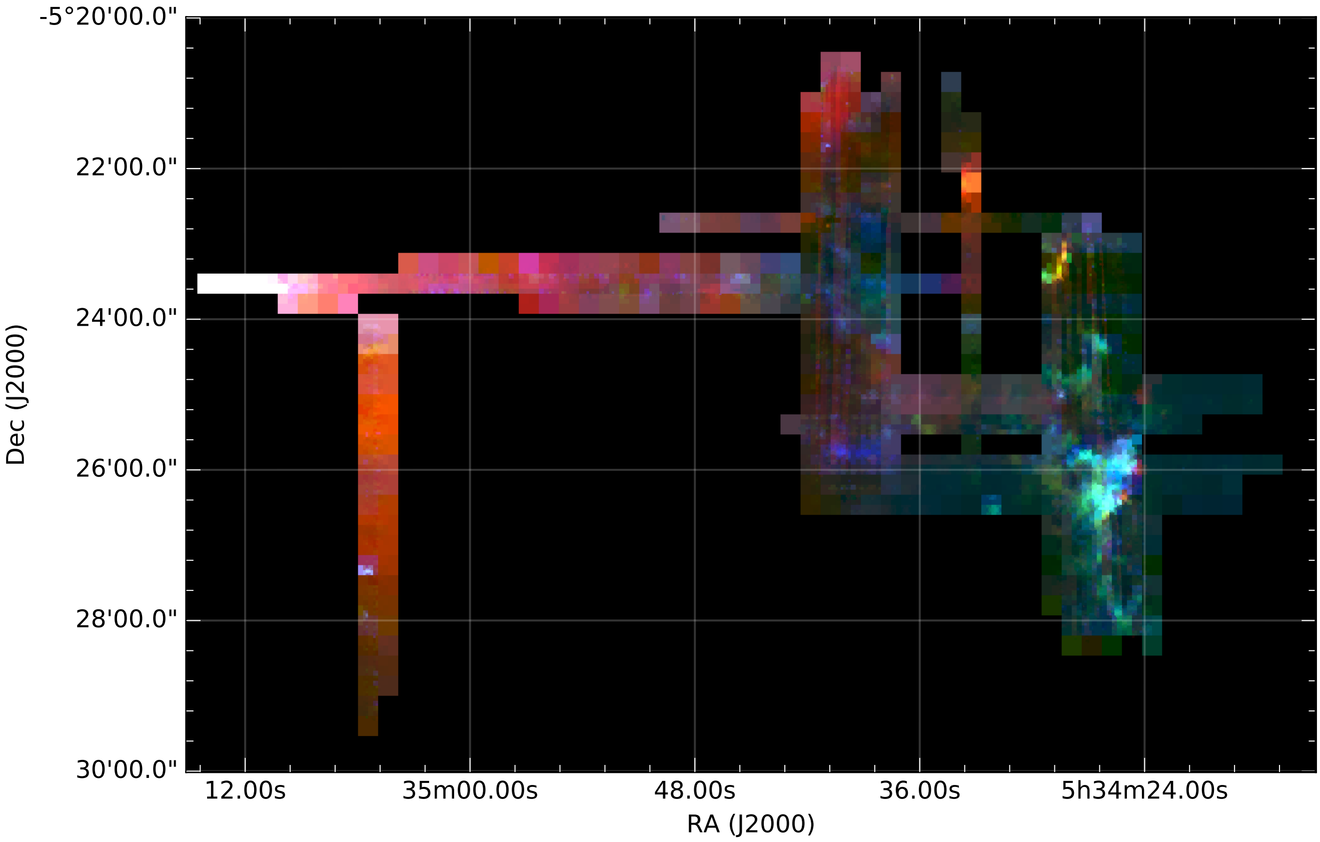

Figure 4. RGB composite image of the western region of the Orion nebula obtained from the Hα isovelocity maps. Red corresponds to the channel maps with heliocentric velocity between -40 and -10 km s^{-1}, blue between -70 and -40 km s^{-1}and green between -110 and -70 km s^{-1}. North is up and east to the left. **(WILL: quitar esta y dejar solo las figuras 5 y 7?)**

Figure 5. Estructuras a gran escala al rojo **(WILL:hacer figura. YO: describir.)**

rich harvest of results that can be subdivided into several distinct topics. First we describe major features seen in the western outskirts of the Orion Nebula. Later we focus on blue and redshifted knots with high radial velocity. In the following sections we provide an empirical description of the kinematical features observed by using the isovelocity channel maps and the position-velocity spectra.

3 LARGE-SCALE STRUCTURES

At least four bow shocks lie in the western part of our observation FoV. These features show velocities slightly redshifted with respect to the systematic velocity of the nebula and their appearance is detected in both Hα and [N II] isovelocity maps. In addition, in order to confirm the identification and make precise locations of the structures we resort to high spatial resolution images obtained from Da Rio et al. (2009) with the WFI (described above), Bally et al. (2006) with the Advanced Camera for Surveys (ACS) of the Hubble Space Telescope and Robberto et al. (2013) also with the ACS (hereinafter D09, B06 and R13). The bow shocks identified are illustrated in Fig. 5. To describe their location we use their positions relative to the feature we will call the Western Wall (WW). **(WILL: describir Western Wall)**.

The largest of the four bow shocks is located on the northeast side of the WW (we identified it as NE red bow shock). It crosses LL2, but is oriented in its opposite direction, towards the west part of the nebula. The channel maps reveal that it is moving with velocities from +0 to +50 km s^{-1} in both Hα and [N II], although some regions show velocities up to 90 km s^{-1} in Hα. The morphology of this bow is very well defined in the high-spatial resolution images from D09, B06 and R13, especially in B06 where it seems to be a region composed of various shocks moving toward the west.

The brighter, west-facing bow shock we identify is located beyond the northwest of the WW (called NW red bow shock) and it seems to mimic the orientation of the northeast one. The bow shock is well defined in Hα, detected at velocities from +10 to +70 km s^{-1}, but is not clear in the [N II] maps, in which there are extended emission at the north of the bow shock moving in the same range of velocities. Attending to the images, this region is spatially coincident only with the observations of D09 and R13, where it can be identified with the brighter emission of the bow shock. However, this feature shows a less well defined bow

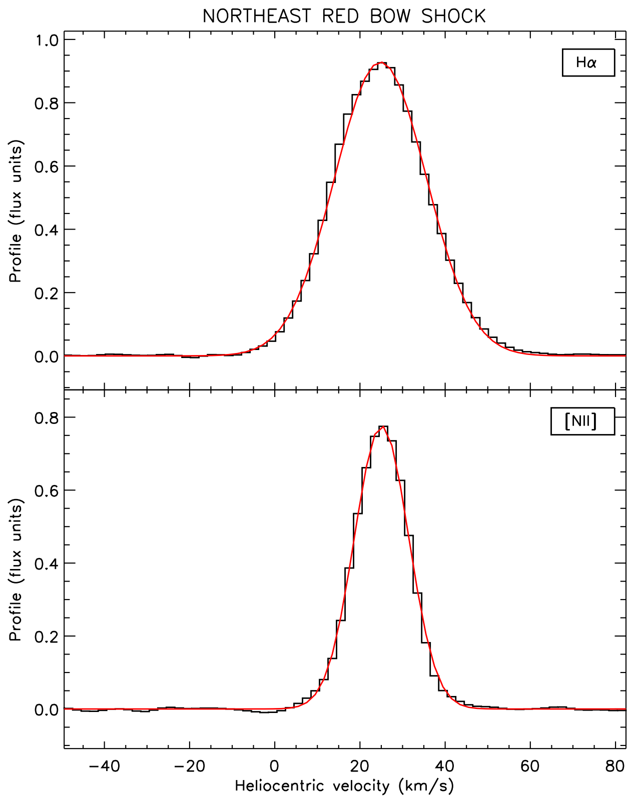

Figure 6. Spectral profiles in Hα and [N II] along the line of sight of the red bow-shock located to the northeast of the Western Wall. The black line represents the profile extracted from the slit spectra after the core subtraction. The red line indicates the Gaussian fit performed.

shape than the others, as if only the edge of the parabolid were detected. This may be because it is located close to the boundary of the WW, where the S/N is lower, preventing the detection the whole bow shock.

On the western side of the WW we identified the third red bow shock (called SW). The composite channel maps show that it is not so redshifted as the other two presented above, moving with velocities from +10 to +50 km s^{-1} in Hα and [N II]. The bow shock structure is clearly identifiable in the images obtained from D09 and R13 and it extends toward the southwest part of the Orion nebula. Analysing the Hα images we observed that in this bow-shock it can be distinguished two orientations: the first one moving to the west (SW-W) and the second one moving to the southwest (SW-S). To check this, the kinematical study of the SW shock will be performed differentiating the two possible sub-shocks.

Finally, the isovelocity maps reveal a red bow shock located to the southeast that is dimmer than the other features described (identified as WE). It is detected in Hα and [N II] maps with velocities ranging from +10 to +50 km s^{-1} and it crosses LL3. The structure of this bow shock is not totally detected in the isovelocity maps because the slit positions observed do not spread enough in the southern part. Nonetheless, the whole bow morphology is perfectly

Table 2. Properties of the red bow-shocks detected in the western region of the Orion Nebula.**(YO: faltan los errores)**

Bow shock	V_{hel} (km s^{-1})		FWHM (km s^{-1})		Flux (Flux units)	
	Hα	[N II]	Hα	[N II]	Hα	[N II]
NE	23.83	24.07	25.41	15.03	12.57	6.21
NW†	25.00	24.96	27.77	12.34	9.44	3.10
SE	21.89	20.63	23.85	15.67	5.03	2.35
SW (S)	24.02	22.52	23.27	14.05	2.76	1.54
SW (W)	21.54	20.91	25.71	17.24	13.39	9.05

† Bad subtraction of the line core.

Figure 7. Mapa con los blue knots identificados **(WILL:hacer figura. YO: describir.)**

identified in the Hα images from D09, B06 and R13.

To estimate the velocity of the shocks we selected those slit positions which cross the bow shocks in representative regions, if possible in areas close to the head of the bow. We found that no slit positions observed in [S II] or [O III] are located near the bow shocks, so we performed this study only in Hα and [N II] emission lines. One-dimensional spectra were extracted in the position of the shocks with an aperture of nine pixels. Nonetheless, the thermal Doppler broadening of the line core (more relevant in Hα than in [N II]) avoids to identify the profile of the shocks (with velocities around +20 km s^{-1}). For this reason, a subtraction of the line core was performed as a background. For each slit position we extracted one-dimensional spectra in two representative regions which were combined by a mean to sample the background variations. These regions were selected as close to perpendicular to shock as possible and in areas outside the bow-shocks to avoid that the emission of the shocked gas dominates the spectrum. Once the line core was subtracted to all the one-dimensional spectra we performed Gaussian fits to the shock profiles weighted by the uncertainties of the background. **(YO: describir calculo de errores)**.

Table 2 lists the properties measured for the four red bow-shocks in Hα and [N II]. Each studied shock is identified in the first column. The second and third columns give the heliocentric velocities measured for the centre of the Gaussian fits. Full width at half maximum (FWHM) are presented in columns 4 and 5, while fluxes obtained from the fits are shown in columns 6 and 7 with their corresponding uncertainties. All the fit performed worked well except for the NW shock where the background profile includes blue shifted emission near the line core making impossible to make a good subtraction on the blue side of the line. Figure 6 shows the spectral profile of one of the red bow-shocks (the northeast one) with the core subtraction and the Gaussian fit performed.

4 HIGH VELOCITY KNOTS

Analysing the position-velocity spectra and the isovelocity maps we detect five redshifted features at high-velocities

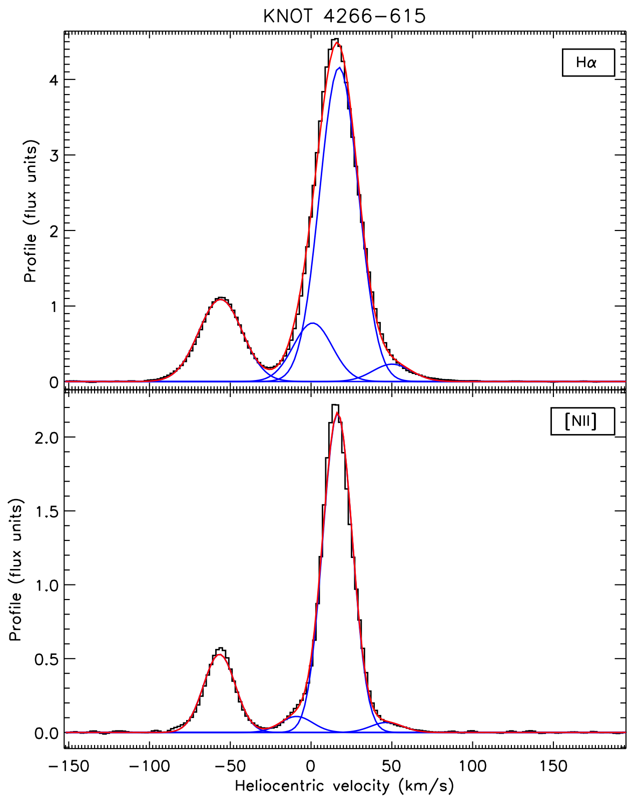

Figure 8. Spectral profile in Hα and [N II] along the line of sight of the blue knot 4266-615. The black line represents the original profile extracted from the slit spectra. The velocity components are represented in blue, while the red line indicates the total fit taking all the components into account.

located nearby to LL1 and LL2, all of them are already catalogued by Henney et al. (2013) and we do not perform any study of them in this work. On the other hand, we find 50 high-velocity blueshifted features in the isovelocity maps. They are distributed over the whole observation FoV, although, as can be appreciated in Fig. 7, there is a concentration of blueshifted knots to the south-west.

We performed a kinematical study of the blue knots for the Hα and [N II] emission lines. The slit positions observed in [S II] and [O III] have a spatial coverage smaller, and only a few knots were detected in these emission lines. For this reason, the study in [S II] and [O III] was performed with different aims than for Hα and [N II], following a different methodology which will be described in the subsection 4.1.

In order to obtain the kinematical properties of the blue knots we resorted to the 2D spectra observed in Hα and [N II]. First, taking the spatial position into account, the knots were identified in the spectra. For those cases in which a knot was sampled by several slit positions, we chose the spectra with better S/N and resolution (i.e. well resolved knots). Then, the one-dimensional spectra were extracted for each knot with an aperture optimized for covering the spatial distribution of the knot minimizing the contamination of adjacent pixels.

To study the one-dimensional profiles we performed Gaussian fits to the line core and the high-velocity component by using our own routines. In the line core we performed a deconvolution into multiple Gaussian components to sample both systematic velocity due to the emission from the ionized layer of the nebula and the light scattered by dust in the photon-dominated region. In the case of the blue knots, their identification depends on their velocity: high-blueshifted components were fitted individually by a Gaussian function while for low-blueshifted features the fit was performed simultaneously with the line core. Fig. 8 shows an example of the fits performed in Hα and [N II].

This procedure was carried out to obtain information in both Hα and [N II] emission lines. However, in some knots the emission in [N II] is too weak and it prevents identification of the features in the profiles. In these cases we consider upper limits to the flux measuring the uncertainty associated with the continuum at the same heliocentric velocity as for the Hα fits. **(YO: describir calculo de errores)**.

Heliocentric velocities, FWHM and fluxes (with their corresponding errors) measured are presented in Table 3 for every detected blueshifted high velocity feature in Hα and [N II]. The last column reports the spatial size of each knot in the orientation of the slit selected to obtain the profile. When naming new compact objects, we have followed the convention established by O'Dell & Wen (1994) that evokes the two-dimensional position on the plane of the sky. The first four digits indicate the position of right ascension and the second three digits the position in declination (both in J2000 epoch and respect to α=5^{h}3X^m:XX^s.X δ=-5°:2X$'$:XX$''$).

4.1 Physical conditions in blue knots

The slit spectra observed in [S II] and [O III] can be used to estimate the physical conditions in the high velocity blueshifted knots. To do that, we first checked how many observed spectra were located over the knots detected in Hα, finding that ten knots were observed in [S II]λλ6717,6731, eight of them also observed in [O III]λ5007. Then, we identified the exact spatial position of every knot in the 2D spectra, and we extracted one-dimensional profiles using the same aperture that for Hα (taking the spatial scales differences into account). Nonetheless, even though the slits were situated over the knots, when analysing the one-dimensional spectra we found that not all the high velocity knots were detected in the profiles. For this reason, the methodology used to obtain the kinematical information and the emitted flux of the knots in [S II] and [O III] was different that the followed in Hα and [N II]. Note that, for both lines, to obtain the flux of the line core the procedure was the same that for Hα and [N II], i.e., a deconvolution into multiple Gaussian components was performed.

In the case of the [S II] emission lines, the knots present shapes far from Gaussian functions, for them we estimated the emission by integrating the flux between two velocity limits (taking as reference the FWHM of the knots in [N II]) and over a fitted local continuum. We were specially careful to select the same velocity range for [S II]λ6717 and [S II]λ6731 to later determine the electron density in an accurate way.

In the case of the [O III]λ5007 the knots were detected without problems in the profiles, thus the blue shifted components were fitted by Gaussian functions to obtain

Table 3. Heliocentric velocities, FWHM, fluxes and spatial sizes for the blueshifted high-velocity knots studied in Hα and [N II]. **(YO:faltan errores)**

Knot	V_{hel} ($\mathrm{km\,s^{-1}}$)		FWHM ($\mathrm{km\,s^{-1}}$)		Flux (Flux units)		Size (arcsec)
	Hα	[N II]	Hα	[N II]	Hα	[N II]	
050-422	-38.91	-38.21	27.06	15.99	2.14	<0.10[a]	4.4
4242-458	-20.90	-22.54	30.59	17.71	4.21	0.91	9.8
4244-554	-16.55	-15.23	28.24	21.23	15.85	8.26	14.2
4245-742	-61.27	-61.96	32.27	14.96	0.47	0.13	3.1
4252-608	-80.10	-82.25	29.17	19.31	0.99	0.44	3.7
4252-616	-16.75	-17.62	37.65	30.12	13.83	7.71	6.9
4254-551	-68.29	-68.67	26.12	17.48	6.41	2.25	8.1
4258-744	-59.53	-62.18	33.56	27.97	2.01	0.66	6.9
4260-612	-64.32	-63.24	38.75	34.10	3.59	1.43	4.4
4261-352	-48.29	-47.96	22.98	14.99	<0.42[a]	<0.11[a]	14.3
4261-422	-57.81	-57.74	35.09	28.40	1.31	0.30	3.1
4261-626	-59.67	-61.19	35.22	26.62	5.05	2.99	5.6
4263-460	-31.88	-32.05	32.94	23.53	1.36	0.27	5.7
4265-630	-54.69	-55.00	34.06	29.13	10.08	3.77	10.6
4266-615	-57.04	-57.68	31.83	23.17	18.44	6.53	16.9
4268-414	-42.08	-41.91	37.92	22.98	0.50	<0.13[a]	3.1
4271-440	-60.68	-64.06	30.20	16.39	1.26	0.40	5.6
4272-545	-64.20	-63.92	28.33	19.96	7.31	2.64	10.0
4272-622	-54.43	-55.64	31.17	21.42	2.53	0.84	6.9
4273-639	-65.21	-64.84	32.94	19.99	0.48	<0.12[a]	4.4
4273-704	-57.61	-64.84	33.26	21.98	1.40	<0.31[a]	16.8
4277-539	-77.01	-77.05	28.24	14.41	0.98	0.23	4.4
4280-551	-72.92	-76.29	27.42	22.45	0.63	0.21	3.7
4284-308	-36.73	-39.87	28.24	20.12	3.42	1.65	5.6
4285-444	-60.15	-59.97	25.87	22.01	0.59	0.12	4.4
4289-524	-71.51	-73.52	25.16	17.25	0.82	0.25	4.4
4289-647	-32.43	-28.28	28.24	20.71	0.50	0.18	4.4
4292-323	-54.91	-56.00	28.58	23.53	3.30	2.29	6.9
4293-557	-41.21	-41.14	32.94	18.83	1.11	0.24	4.8
4320-626	-64.73	-65.89	27.27	12.33	1.54	0.27	6.9
4331-453	-30.21	-32.39	28.24	18.83	1.63	0.35	6.8
4332-401	-71.00	-69.93	15.27	13.83	0.15	0.07	3.1
4334-560†	-67.06	-72.08	16.64	17.10	0.16	0.09	5.6
4335-207†	-19.36	-21.52	27.50	15.61	94.23	25.53	23.0
4359-521	-37.34	-38.58	31.18	16.00	1.90	0.35	6.9
4374-457†	-66.67	-67.16	24.58	14.99	0.19	<0.03[a]	2.6
4376-329	-79.92	-81.66	26.27	15.68	0.49	0.13	4.3
4377-526	-70.96	-71.50	28.24	13.30	0.52	0.07	3.7
4378-434	-68.00	-68.44	28.24	16.99	0.22	<0.03[a]	4.3
4381-411	-67.31	-69.64	30.71	17.17	0.44	0.05	3.1
4383-343	-63.12	-65.41	38.22	16.46	0.40	0.07	3.1
4385-243	-77.62	-78.31	31.38	18.99	0.33	<0.03[a]	5.6
4389-327	-63.03	-65.38	44.71	15.99	0.67	<0.15[a]	6.8
4396-541	-90.00	-91.25	23.59	13.72	0.87	0.11	8.1
4402-400	-75.26	-78.97	23.53	13.15	0.54	0.12	5.6
4405-349	-78.13	-77.93	20.73	15.99	0.14	<0.04[a]	4.3
4406-330	-68.93	-69.20	23.53	13.99	0.27	<0.03[a]	5.6
4407-229	-78.61	-80.39	25.93	11.72	0.19	0.04	4.4
4409-243	-67.17	-66.78	22.16	12.99	0.18	<0.02[a]	5.6
4456-324	-68.95	-71.43	19.23	8.99	0.74	<0.14[a]	6.8

† Knots with uncertain identification and fits.

[a] Upper limits intensities obtained by measuring fluxes below the line.

the emitted fluxes. This procedure was carried out in all the knots with the exception of 4261-352 in which the emission was too weak and we determined the flux by integrating the uncertainties associated with the continuum. It is interesting to emphasise the behaviour of the knot 4261-352. Initially, this knot was not identified because it does not emit in Hα or [N II]. However, when analysing the 2D spectra in [S II] we found a weak, but not negligible, emission in [S II]λ6731 at $V_{\mathrm{hel}} \sim$ -48 $\mathrm{km\,s^{-1}}$, undetected hitherto. This is the single case of the 50 blue knots studied

Table 4. Association between our blueshifted knots and the slit positions observed by O'Dell & Harris (2010). Extinction coeficient and electron temperature presented are the values derived by OH10.

Knot	OH10's slits	c(Hβ)	T_e([N II]) (10^4K)	T_e([O III]) (10^4K)
050-422	11-West	0.26	0.84	0. 78
4254-551	D-North/D-NE	0.005	0.88	0.92
4258-744	D-North	0.01	0.86	0.92
4261-352	D-North	0.01	0.86	0.92
4261-422	D-North	0.01	0.86	0.92
4261-626	D-North/D-NE	0.005	0.88	0.92
4263-460	D-North/27-West	0.01	0.88	0.94
4331-453	27-West	0.01	0.89	0.97
4332-401	27-West	0.01	0.89	0.97
4334-560	D-NE	0.0	0.89	0.92

in which the flux was not measured by performing Gaussian fits in any emission line, it was always determined by integrating the flux at the same heliocentric velocity range as for the [S II]λ6731 emission line.

To determine the real line intensity emitted by each blueshifted knot it is important to correct for the effects of foreground dust extinction. With our observations we have not information about the Balmer lines necessary to obtain the extinction coefficient c(Hβ). O'Dell & Harris (2010) (hereinafter OH10) performed long slit observations in the Orion Nebula, in particular, four of their slit positions cross the blue knots studied in this section or are located near of them. We decided to adopt their values of c(Hβ) to de-redden our emission lines. In Table 4 we show the association between OH10 slit positions and our knots; in those knots that are close of two slits we consider the average value of both. As can be seen, the extinction coefficient presents values near to zero for all the knots (except for 050-422), therefore this approximation has an insignificant effect on the corrected fluxes. Table 5 lists the reddening-corrected intensities of the emission lines measured for every blue knot relative to Hα. Intensities were derived using the same values of the reddening function f(λ) that OH10.

The electron density (n_e) was determined from the nebular doublet ratio [S II]λ6717/[S II]λ6731 using the IRAF package TEMDEN based on a five-level statistical equilibrium model (De Robertis et al. 1987; Shaw & Dufour 1995). To estimate n_e, electron temperature (T_e) is requiered, but in this work no emission lines necessary to derive T_e have been observed. Because of it we resorted again to the observations of OH10 to determine T_e from the line intensities of the slits which cross our knots. Although the line intensities that they present in the paper were obtained by integrating the flux over the whole slit, to adopt their values is not a bad approximation because the nebula does not present strong variations in T_e (as can be seen in columns 4 and 5 of Table 4); in addition, the density dependence with the temperature is very small, e.g., variations in T_e from 0.8×10^4K to 1.2×10^4K increase n_e less than 100cm^{-3} (which is in the range of the intrinsic uncertainties of the line measurements).

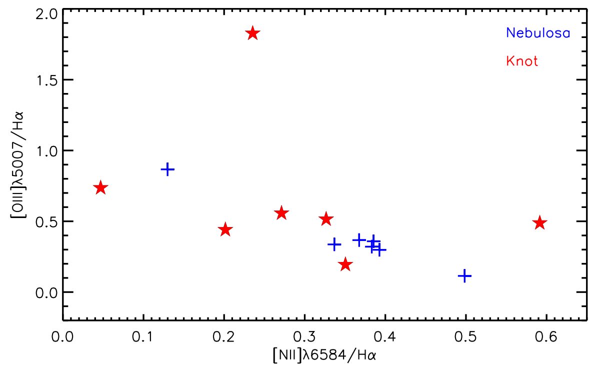

Figure 9. Diagrama Diagnostico provisional. Hay una nueva versiÃşn. Mejorar

The physical parameters were derived by performing an iterative process for each knot until achieving agreement between the electron density and electron temperature. We used our own measurements of the [S II] line ratio to estimate n_e and OH10 measurements to derive T_e (all the line intensities were de-reddened under the same conditions). The values of n_e inferred for each knot are shown in Table 5, as well as T_e([N II]).

(YO: Falta descripcion de calculo de errores en toda esta subseccion).

4.2 Diagnostic diagrams

Describir obtencion de flujo para la nebulosa.
Explicar figura 9
Analizar resultados

5 POINT OBJECTS

Pensar si poner esta secciï£¡n o si no merece la pena

6 DISCUSSION

7 CONCLUSIONS

ACKNOWLEDGEMENTS

REFERENCES

Bally, J., Licht, D., Smith, N., & Walawender, J. 2006, AJ, 131, 473

Da Rio, N., Robberto, M., Soderblom, D. R., et al. 2009, ApJS, 183, 261

De Robertis, M. M., Dufour, R. J., & Hunt, R. W. 1987, J. R. Astron. Soc. Canada, 81, 195

Henney, W. J., García-Díaz, M. T., O'Dell, C. R., & Rubin, R. H. 2013, MNRAS, 428, 691

Meaburn, J., López, J. A., Gutiérrez, L., et al. 2003, Rev. Mex. Astron. Astrofis., 39, 185

O'Dell, C. R., & Harris, J. A. 2010, AJ, 140, 985

Table 5. Reddening corrected line ratios and physical parameters derived for the blue-knots. **(YO: faltan errores)**

Knot	[O III]λ5007/Hα	[N II]λ6584/Hα	[S II]λ6717/Hα[b]	[S II]λ6731/Hα[b]	R_{S2}	T_e([N II])[c] (10^4K)	n_e([S II]) (cm^{-3})
050-422	0.74	<0.05[a]	0.01†	0.02†	0.55	0.90	4964
4254-551	0.19	0.35	0.03	0.03	0.98	0.88	600
4258-744	0.51	0.33	0.04	0.03†	1.41	0.86	<100
4261-352	<0.56[a]	<0.27[a]	0.08†	0.65	0.12	0.86	-
4261-422	0.70	0.23	0.08	0.07	1.19	0.86	242
4261-626	0.49	0.59	0.21	0.26	0.80	0.88	1197
4263-460	0.44	0.20	0.04	0.05†	0.83	0.87	1078
4331-453	-	0.22	0.08	0.14†	0.59	0.88	3627
4332-401	-	0.44	0.18	0.14	1.35	0.88	<100
4334-560	-	0.57†	0.14	0.17	0.84	0.91	1014

† Knots with uncertain identification and fits.

[a] Upper limits intensities obtained by measuring fluxes below the line.

[b] Sulphur lines were all obtained by integrating the flux between two velocity limits.

[c] Derived by adopting the lines intensities from OH10.

O'dell, C. R., & Wen, Z. 1994, ApJ, 436, 194
Robberto, M., Soderblom, D. R., Bergeron, E., et al. 2013, ApJS, 207, 10
Shaw, R. A., & Dufour, R. J. 1995, PASP, 107, 896
Weilbacher, P. M., Monreal-Ibero, A., Kollatschny, W., et al. 2015, A&A, 582, A114

This paper has been typeset from a TEX/LATEX file prepared by the author.